ORIGINAL ARTICLE

Microstructure characteristics and mechanical properties of stationary shoulder friction stir welded 2219-T6 aluminium alloy at high rotation speeds

Jiaqing You [1,2] · Yunqiang Zhao [2] · Chunlin Dong [1,2] · Chungui Wang [2] · Shu Miao [2] · Yaoyong Yi [2] · Yunhai Su [1]

Abstract

Stationary shoulder friction stir welding has been used to weld 4-mm-thick 2219-T6 aluminium alloy at high rotation speeds. Strain plastic damage was applied to demonstrate the formation mechanism of welding defects at high rotation speeds above 2000 rpm. A three-way converging zone in the joint, in which materials of different microstructure characteristics converged from three directions during high tool rotation speed welding, was found. At the relatively high tool rotation speed, the significant differences in the microstructures would result in weld defects in this zone. It could be attributed to material toughness damage at high strain rate. With increasing tool rotation speed, the tensile strength of the joint constantly decreased. When the tool rotation speed varied from 2000 to 2600 rpm, the tensile strength decreased from 305 MPa (68.2% of the BM) to 238 MPa (53.2% of the BM).

Keywords Stationary shoulder friction stir welding · Three-way converging zone · Microstructure · Mechanical properties

1 Introduction

Friction stir welding (FSW) is a solid joining technology with the characteristics of high welding efficiency, good joint quality and no pollution. It has been widely applied in many industries, such as aviation, aerospace, rail trains and ships [1–3]. To improve the weld appearance, stationary shoulder friction stir welding (SSFSW) was invented. In the SSFSW, the shoulder and pin are separated. In the course of welding, only the pin is rotated. As a result, flash and fish scales can be eliminated by the stationary shoulder [4–5].

✉ Yunqiang Zhao
  zhaoyq@gwi.gd.cn

✉ Chunlin Dong
  dongchl@gwi.gd.cn

1 Department of material science and engineering, Shenyang University of Technology, Shenyang 110870, Liaoning, China

2 Guangdong Welding Institute (China-Ukraine E.O. Paton Institute of Welding), Guangdong Provincial Key Laboratory of Advanced Welding Technology, Guangzhou 510651, China

Compared with conventional FSW, the welding heat input for the SSFSW is low because no rotation friction occurs for the stationary shoulder. Therefore, joint softening can be reduced, and the mechanical properties of the joint can be improved [6–8]. Wu et al. [9] investigated the microstructures and mechanical properties of joints welded by FSW and SSFSW. Their results indicated that the heat input of SSFSW was 30% lower than that of FSW, and a narrower heat-affected zone (HAZ) and thermo-mechanically affected zone (TMAZ) were obtained. However, the correlation between microstructures and mechanical properties was not explained in detail. Sun et al. [10] characterised the residual stress distribution and texture evolution in AA7075 SSFSW joints. The study indicated that the material flow had great influence on the residual stress and texture. Li et al. [11] also studied the SSFSW of 2219-T6 aluminium joints. According to their study, the maximum tensile strength reached 69% of base material at 800-rpm rotation speed. When the rotation speed increased to 1000 rpm, a cavity defect was formed; this resulted in the joint tensile strength dramatically decreasing. Li et al. [12] reported that the 750–1500-rpm tool rotation speeds apparently increased the widths of NZ, TMAZ, and HAZ in AA6061-T6 aluminium alloy joints, while the influences of 100–300-mm/min welding speeds on the width of

NZ were weak. These results indicated that the effects of rotation speed on the microstructures were more significant.

To meet the needs of intelligent manufacturing, FSW technology should be combined with industrial robotics. In the case of robotic SSFSW, large torque induces robot overload due to the low stiffness of the robot. This adverse restricts the development of robotic SSFSW. Hosain [13] pointed that the welding torque could be decreased by increasing the tool rotation speed at a constant welding power. Therefore, high–rotation speed SSFSW combined with industrial robots is a promising technology. In recent, most studies on SSFSW are focused on relatively low rotation speeds in a 600–1500-rpm range [9–12]. Stationary shoulder friction stir welding of aluminium alloy at high rotation speeds is not reported in detail.

The aim of this work is to study stationary shoulder friction stir welding of 2219-T6 aluminium alloy at high rotation speeds. The weld formation, microstructures and mechanical properties of high–rotation speed SSFSW joints were investigated in detail.

2 Experimental procedures

The base material (BM) used in the experiments was 4-mm-thick 2219-T6 aluminium alloy plate, 220 mm long by 80 mm wide. The nominal chemical composition is shown in Table 1.

The welding experiments were carried out on the integrated system of the KUKA machine (KR 1000 titan) and PLC control cabinet (s7-1500PLC). Figure 1 illustrates the self-designed tool system, which can be divided into two main parts, the stationary shoulder and tool pin. The inner and outer diameters of the stationary shoulder are 8 mm and 14 mm, respectively. The tool pin employs conical-thread design with auxiliary shoulder, and the diameter of that is 8 mm. The tool pin length is 3.9 mm, and the bottom and top diameter of it are 5 mm and 4 mm, respectively. The welding direction was parallel to the rolling direction, and the tilt angle of the tool with respect to the z-axis was 2.5°. The groove defects appeared at 1800-rpm rotation speed, so the welding speed was fixed at 100 mm/min and the rotation speed varied in the 2000–2600-rpm range.

After welding, microstructures and Vickers hardness tests were investigated. A transverse section sample was cut perpendicular to the welding direction. The sample was ground, polished and etched using Keller's reagent (2.5%HNO₃, 1%HF, 1.5%HCl, 90%H₂O, volume fraction). Then, the microstructures were observed using an optical microscope (OM, Axio Imager M2m). The Vickers hardness was tested

using the Vickers hardness tester (WILSON VH1202) with a 300-g load for 10 s. The tensile samples, with a gauge length of 25 mm and a width of 6 mm, were prepared according to China National standard GBT 16865-2013(equivalent to American Standard ASTM E8). The tensile test was carried out at room temperature using a universal tensile machine at a constant 2 mm/min. For each welding parameter, three tensile duplicates were tested. The textural evolution and fracture microstructures were examined on the cross section of the SSFSW joint by electron backscattering diffraction (EBSD) using a Zeiss-Merlin scanning electron microscope (SEM). Before the EBSD testing, the specimens were ion beam-polished for 1 h on a Leica EM TIC 3× ion beam milling system after sanding and mechanical polishing. The parameters are 4.5 kV, 4 kV, 3.5 kV and 3 kV. Each parameter works for 15 min.

3 Results and discussion

3.1 Weld formation and microstructures

Figure 2 shows the weld formations of SSFSW varying from 2000 to 2600 rpm. All welds have smooth surface appearances and no flash defects, and little weld thinning can be observed, as shown in Fig. 2 a and c. The non-rotating shoulder can smooth the surface and prevent material loss at high rotation speeds. Figure 2 b and d show the cross sections of SSFSW joints at 2000 and 2600 rpm, respectively. The joints are divided into BM, HAZ, TMAZ and NZ. The width of the NZ and HAZ increases with increasing tool rotation speeds. It can be concluded that when the tool welding speed is constant, a higher rotation speed causes larger heat input and more drastic plastic flow. Wu et al. [9] also found the same phenomenon by using thermal and hardness modelling. Therefore, the joints have larger plastic deformation and strain rate at 2600 rpm.

Figure 3 shows the microstructures in the NZ near the advanced side (AS) of SSFSW joints at different rotation speeds. A three-way converging zone (TCZ) is formed in the observed zone. With the help of the assisted shoulder and the pin, the material at the top of the workpiece moves down, while the material at the bottom moves up. Meanwhile, the plastic material in the NZ undergoes a helical motion. In this zone, materials with different microstructure characteristics converge from three directions. The grains at the bottom of the TMAZ are elongated upward, while the grains at the top of the TMAZ are elongated downward, as shown by the arrows

Table 1 Nominal composition of 2219-T6

| Cu	Mn	Si	Zr	Fe	Mg	Zn	V	Ti	Al
5.8~6.8	0.2~0.4	≤ 0.2	0.1~0.25	≤ 0.3	≤ 0.02	0.10	0.05~0.15	0.02~0.1	Bal

Fig. 1 SSFSW tool and welding machine
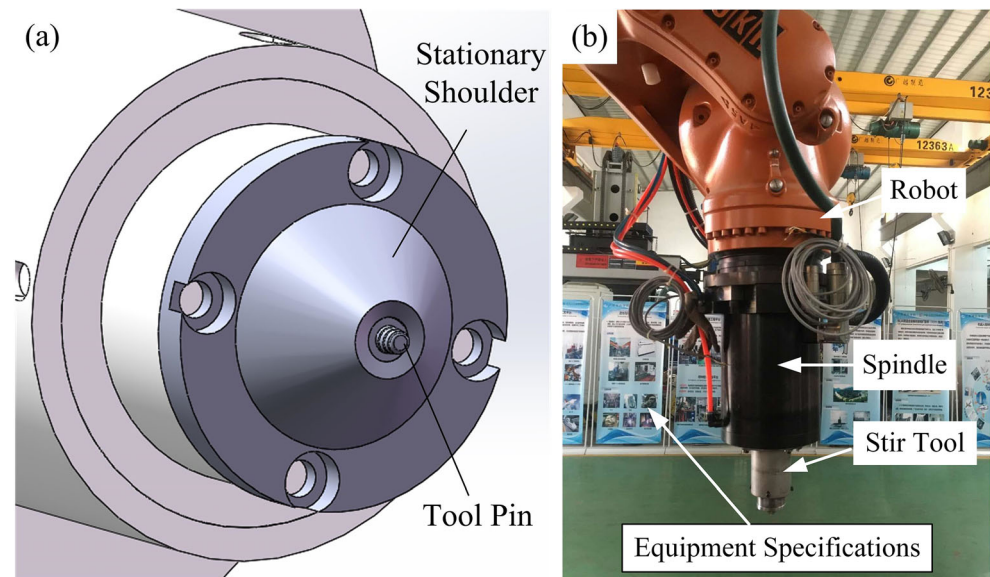
in Fig. 3a. The grains in the NZ are equiaxed fine grains, which can be attributed to the occurrence of dynamic crystallisation [14]. According to the previous studies, the formation of the TCZ is attributed to the different material flow and plastic deformation near the converging area. It should be noted that the microstructure difference increases with increasing rotation speed, and crack defects tend to form in the TCZ (as seen in Fig. 3d). For most previous studies on conventional FSW or SSFSW, only void defects, which are usually formed at a low rotation speed, were studied. However, crack defects for SSFSW at high rotation speed have not been studied. Therefore, the formation mechanism of crack defects was discussed in detail in this study.

The differences in material plastic deformation in the TCZ have an effect on crack initiation. The microstructure in the TCZ was observed by EBSD to analyse plastic deformation behaviour, as shown in Fig. 4. The pole figures are computed from EBSD mapping results and each region, A, B and C, associated with Fig. 4e–g. The three regions have quite different morphologies and different grain sizes. Region A has the characteristic of grain growth compared with grains in the NZ. The average grain size is 6.5 μm, which is due to the welding thermal cycle. Lath-shaped grains with a 5.7-μm average are elongated

by the geometrical requirements of the imposed strain in region B. The grains in region C are fine and equiaxed due to adequate stirring of the pin. The average grain size is 3.8 μm; this indicates that the materials undergo dynamic recovery and dynamic recrystallization.

The pole figures indicate that the textures in the regions A, B and C are significantly different (as seen in Fig. 4e–g) according to the pole figures of ideal simple shear orientations for the {111} plane of FCC materials, as shown in Fig. 5 and Table 2. Table 3 shows the dominating textural components and strength of A, B and C regions. Distributions of the orientation peaks in region A contain $(11\bar{1})[1\bar{1}0]$, $(100)[0\bar{1}1]$ and $(\bar{1}\bar{1}2)[\bar{1}10]$ components, and the dominating textural components are $(11\bar{2})[1\bar{1}0]$ and $(11\bar{1})[1\bar{1}0]$ in region B. For region C, the texture component strength is weaker, and the component is very close to the $(\bar{1}\bar{1}2)[\bar{1}10]$ simple-shear textural component. The different textural components illustrate that the materials in different regions undergo different plastic deformation [15–16]. Furthermore, materials in regions A and B have the characteristic (111) [110] simple-shear texture. According to Hu [17], this characteristic tends to be developed at low strains. Region C presents the characteristic (112) [110] simple shear texture; it should be
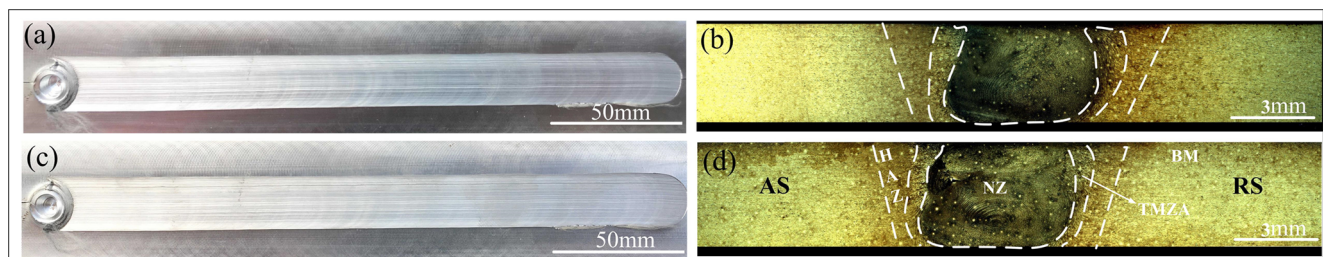
Fig. 2 Surface appearance and cross section of SSFSW joints at 2000 and 2600-rpm rotation speeds. **a** Surface appearance at 2000 rpm. **b** Cross section at 2000 rpm. **c** Surface appearance at 2600 rpm. **d** Cross section at 2000 rpm

Fig. 3 Grain structures at the
interface between AS and NZ. a
2000 rpm. b 2200 rpm. c 2400
rpm. d 2600 rpm
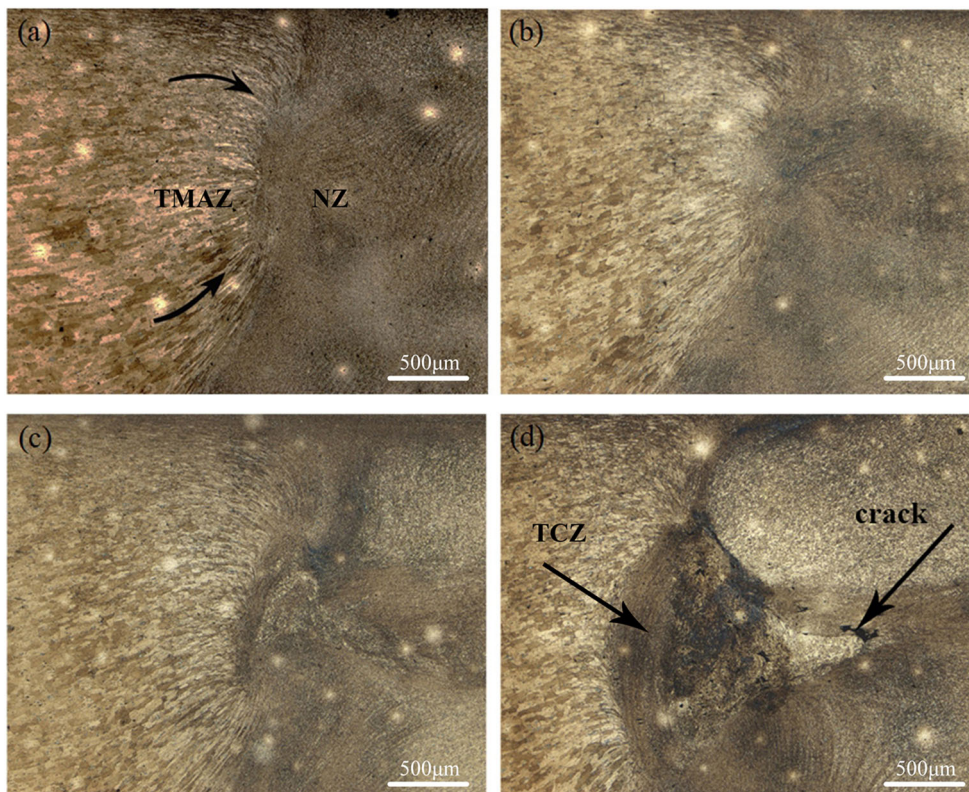
developed at high strains. In addition, the textural peaks in the PFs are slightly deviated from the ideal positions because of the 2.5° tool titling and the threads on the probe surface.

As shown in Fig. 6, the BM consists of 65.2% low-angle boundaries (LABs). Most LABs have misorientation angles smaller than 5°. Misorientation angles of the high-angle boundaries (HABs) are concentrated at 40°. After SSFSW, numerous LABs are generated in the grain interior, as shown in Fig. 6b, c. In contrast to the BM, the LAB fraction increases to 82.4 and 81.2%, respectively. However, the fine grains in region C are surrounded by HABs. The LAB fraction decreases to 57.5%. The HABs are more uniform due to
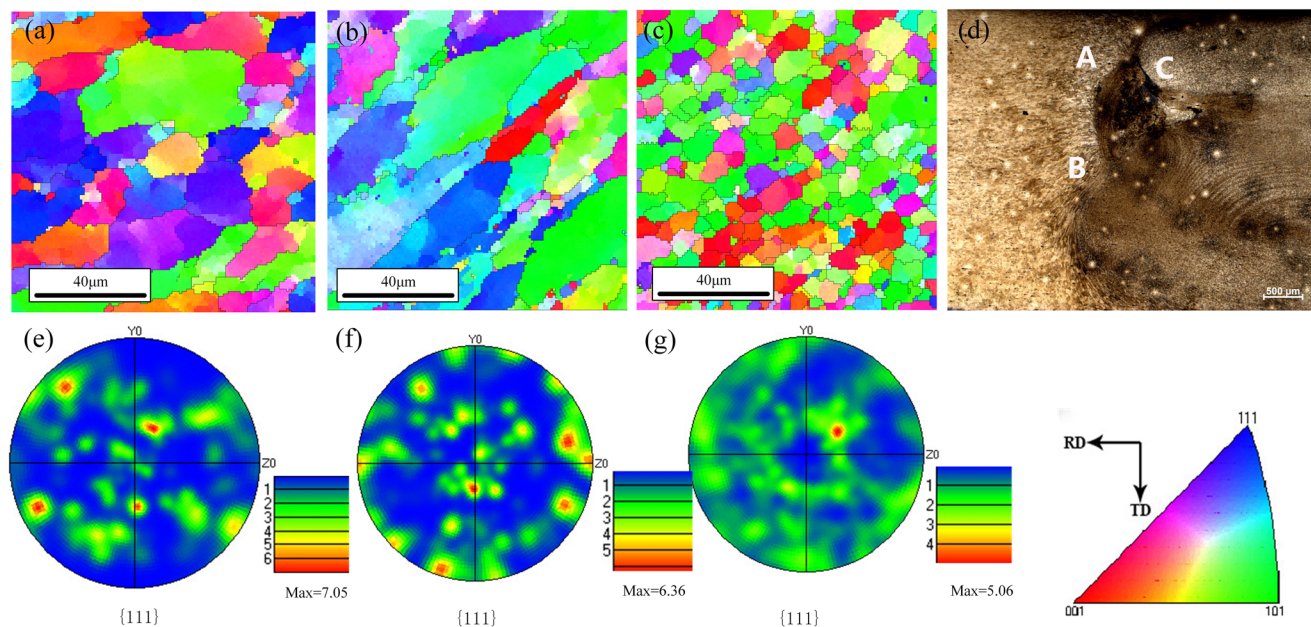
Fig. 4 EBSD maps and pole figure maps of three-way converging zone across the welding direction. EBSD step size is 0.8 μm. a and e Area A in the TCZ. b and f Area B in the TCZ. c and g Area C in the TCZ
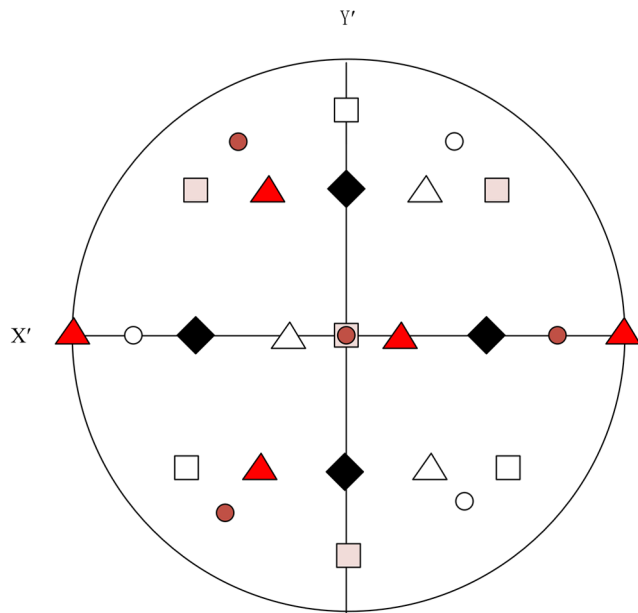
Fig. 5 Pole figures of ideal simple shear orientations for the {111} plane of FCC materials [18]

dynamic recrystallization. It is demonstrated that grains undergo different plastic deformation in the area, resulting in the formation of the TCZ.

3.2 Microhardness distribution

The transverse cross-sectional hardness contour maps of the SSFSW joints at different rotation speeds are depicted in Fig. 7. The hardness gradient is obvious. The hardness of BM is in

Table 3 The texture components of the TCZ

| Area	Miller indices	Strength
A	$(11\bar{1})\,[1\bar{1}\,0]$, $(100)\,[0\bar{1}1\,]$, $(\bar{1}\,\bar{1}2)\,[\bar{1}10\,]$	7.05
B	$(11\bar{2})\,[1\bar{1}0\,]$, $(11\bar{1})\,[1\bar{1}\,0]$	6.36
C	$(\bar{1}\,\bar{1}2)\,[\bar{1}10]$	5.06

the range of 125–135 Hv, the softened region contains the HAZ, TMAZ and NZ, and this is the result of grain evolution affected by welding thermal cycle and precipitation. The NZ hardness is higher than that of the TMAZ due to equiaxed grain structures. The grains undergo an ageing strengthening process, with the second phase particles dissolved and re-precipitated in the NZ. Meanwhile, the original grains are broken by the rotating pin. As a consequence, the number of boundaries is increased [19–20]. The joints welded at 2000 rpm have the smallest HAZ and NZ among all joints at different rotation speeds, owing to the lower heat input. The minimum microhardness value appears at the interface between TMAZ and NZ. With further increasing of the rotation speed to 2200 and 2400 rpm, the softened region profile increases gradually. Compared with the joint welded at 2000 rpm, the microhardness in the NZ increases slightly at 2600 rpm.

3.3 Tensile properties and fracture characteristics

Figure 8 shows the tensile properties of joints produced at different rotation speeds. When the tool rotation speed varies from 2000 to 2600 rpm, the tensile strength of the joint constantly

Table 2 Ideal orientations of important simple shear texture components [18]

| fcc ideal simple shear nomenclature		Euler angle		
component	Miller indices	$\phi 1$	Φ	$\phi 2$
•	$(11\bar{1})\,[1\bar{1}0]$	180	55	45
○	$(\bar{1}\bar{1}1)\,[\bar{1}10]$	0,360	55	45
▨	$(11\bar{1})\,[2\bar{1}1]$	30,210	55	45
□	$(1\bar{1}1)\,[\bar{2}\bar{1}1]$	150,330	55	45
▲	$(11\bar{2})\,[1\bar{1}0]$	180	35	45
△	$(\bar{1}\bar{1}2)\,[\bar{1}10]$	0,360	35	45
◆	$(100)\,[0\bar{1}1]$	45,135,225,315	0,90	0
		0,180,360,	45	0
		0,180,360	0	45
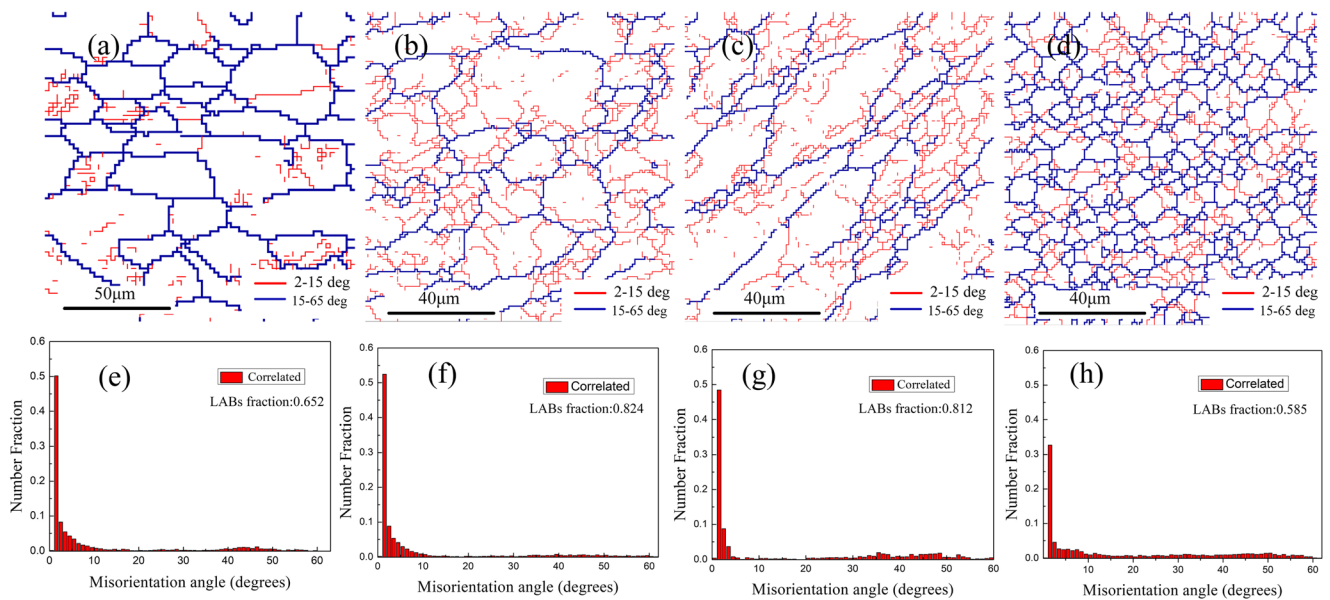
Fig. 6 Microstructural features of the base material (**a**, **e**) and three-way converging zone (**b–d**, **f–g**). **a–d** Grain boundary map. **e–h** Misorientation distribution. **b**, **f** Maps of region A. **c**, **g** Maps of region B. **d**, **h** Maps of region C

decreases from 305 to 238 MPa. The tensile strength of the 2000-rpm joints reaches the maximum value of 305 MPa, equivalent to 68.2% of that of the BM. The tensile strength value of the 2600-rpm joints is lowest due to cracks in the TCZ, as shown in Fig. 3.

Figure 9 shows the cross sections of the tensile fracture joints at different rotation speeds. It can be clearly seen that the tensile specimens fractured were in the NZ at the 2000-rpm tool rotation speed. It is attributed that materials near the bottom surface could not be completely broken by the tool pin at 2000 rpm. This phenomenon has also been founded in the previous study [17]. The tensile fracture path shows a 45° angle to the tensile axis, as a typical shear fracture pattern. The specimens are shown in Fig. 9b–d fracture in the TCZ. The crack propagates along the interface between the TMAZ and the NZ in Fig. 3a. The specimen at the 2600-rpm rotation speed shows fractures along a crack in the TCZ, and the tensile strength dramatically decreases due to sub-size cracks.

Figure 10 shows the fracture surface of the tensile specimens machined from the joints at different rotation speeds. A large number of deep dimples with obvious tearing edges on their sidewall are seen, as shown in Fig. 10a. The dimples include the larger primary ones (see type A) and the surrounding smaller secondary ones (see type B), which is a typical characteristic of ductile fracture [21]. The larger primary dimples resulted from the second phase particles stripping. The smaller secondary dimples resulted from the voids nucleating in impurities and the weaker areas of the materials discussed above [22]. The number of dimples in the fracture surface decreases gradually with increasing strain rate. Less ductile dimples and a sub-size cleavage surface (see type C) can be observed in Fig. 10d. According to the micropore aggregation fracture mechanism, the welded fracture surfaces 2600 rpm belong to quasi-cleavage fractures. This phenomenon indicates that the crack is the main reason for the decrease of tensile strength.
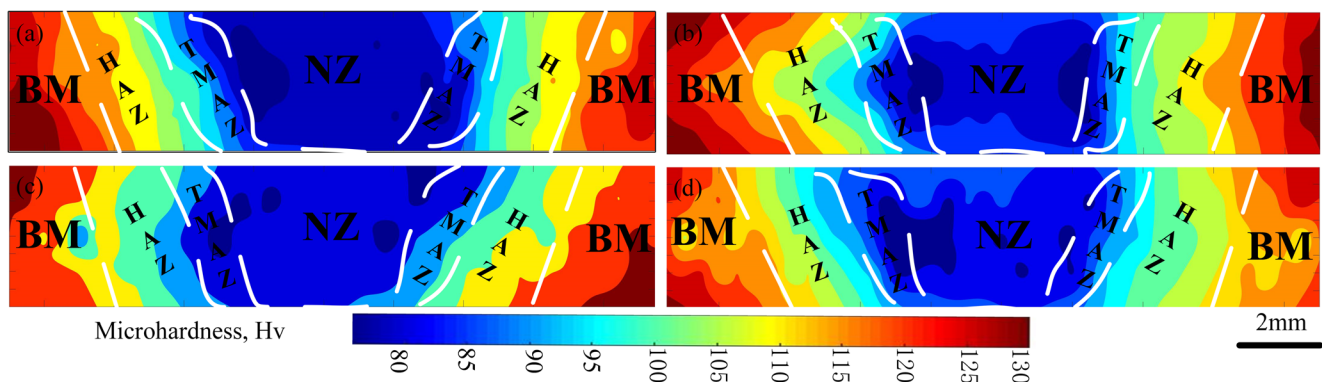
Fig. 7 Cross-sectional hardness contour maps from welds produced with SSFSW at different parameters. **a** 2000 rpm. **b** 2200 rpm. **c** 2400 rpm. **d** 2600 rpm

**Fig. 8** Tensile properties of joints welded by SSFSW at different tool rotation speeds
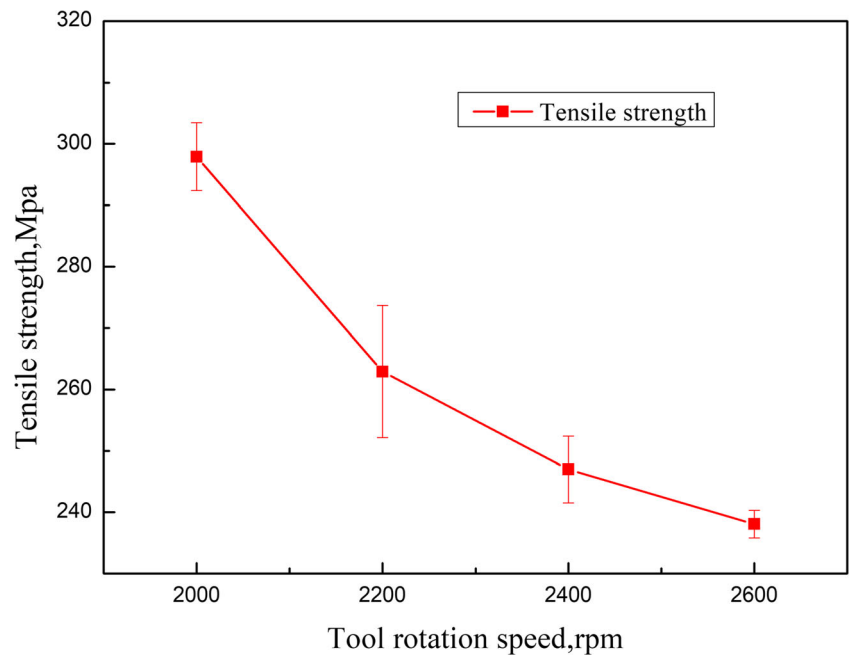
4 Discussion

### 4.1 The formation mechanism of cracks at high rotation speed

For conventional FSW, a cavity defect is liable to form in the TCZ when the rotation speed is not appropriate. The reason for the cavity formation is due to insufficient material fluidity at low rotation speed or material loss at high rotation speed [15]. But for the SSFSW, there is no material loss. Therefore, the crack under the high-speed rotation is not caused by material loss. Strain plastic damage accounts for crack initiation in the TCZ. Previous works indicated that ductile damage occurred during material

Fig. 9 Macroscopic images of the tensile fracture joints welded by SSFSW at different rotation speeds. **a** 2000 rpm. **b** 2200 rpm. **c** 2400 rpm. **d** 2600 rpm
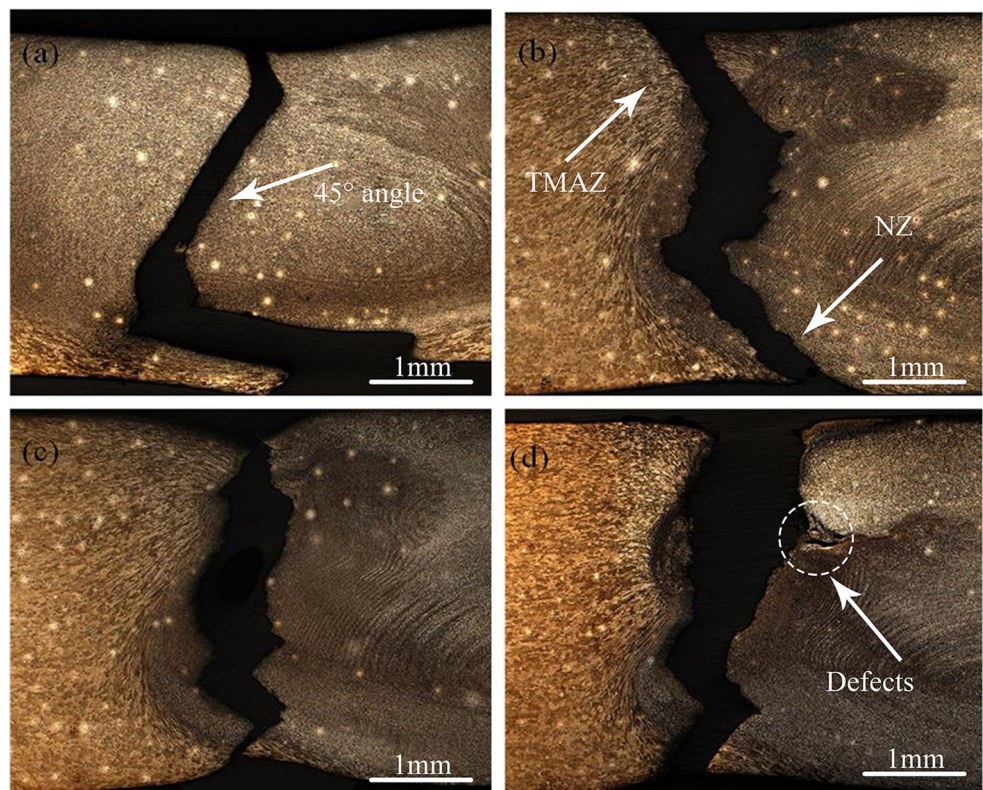
Fig. 10 SEM micrographs showing tensile fracture surface characteristics of the joints at different rotation speeds. **a** 2000 rpm. **b** 2200 rpm. **c** 2400 rpm. **d** 2600 rpm
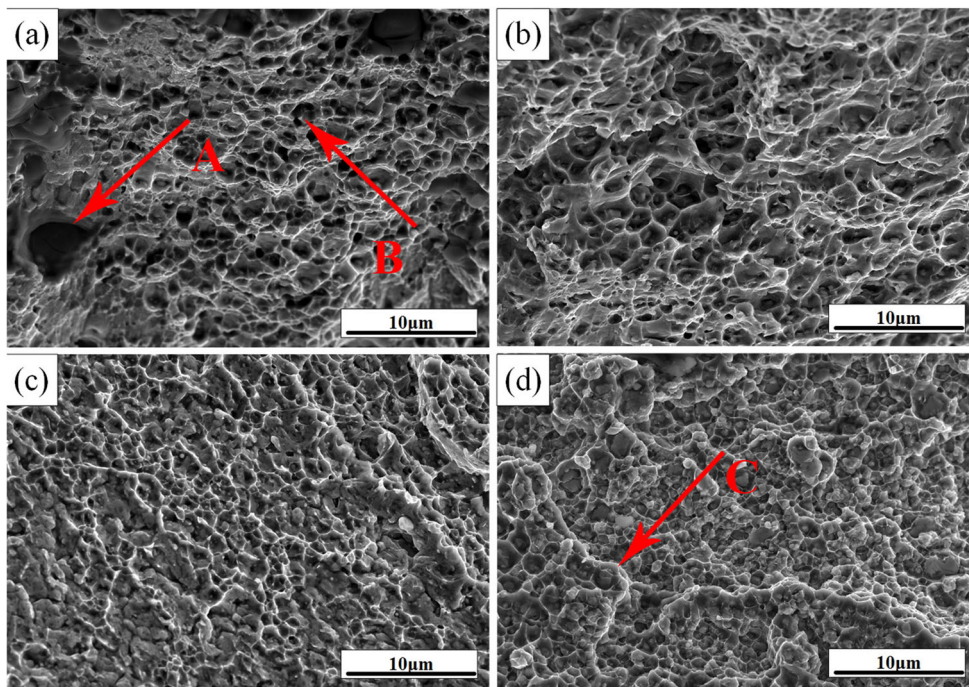
formation at high strain rates, and then, micropore nucleation accumulated to form defects [23]. Argon and Goods [24–25] investigated the relationship between micropore nucleation volume rate and strain rate, and formulated the following Eq. (1):

$$f^*_N = A\left(\sigma^*_m + \frac{1}{3}\sigma^*_{kk}\right) + B\varepsilon^{*p}_m \tag{1}$$

When the nucleation was controlled by strain rate:

$$A = 0$$
$$B = \frac{f_N}{S_N\sqrt{2\pi}}\exp\left\{-\frac{1}{2}\left(\frac{\varepsilon^p_m - \varepsilon_N}{S_N}\right)^2\right\} \tag{2}$$

where A and B are normally distributed functions, f^*_N is the micropore nucleation volume rate, f_N is the micropore nucleation volume factor, S_N is the standard deviation, ε_N is the nucleation strain threshold and ε^p_m is the equivalent plastic

strain. The micropore nucleation rate increases with increasing strain rate, which results in more serious plastic damage. In this study, the gradually increasing rotation speed leads to increasing material strain rate. Then, a lot of cracks initiate and propagate. Meanwhile, heat input at the same rotation speed is no different in the TAC [26]. Liu [27] stated that the TCZ area has the maximum strain rate in the welded joints. This is also the reason for the large difference in the microstructures of the TCZ, which is consistent with the results analysed by EBSD.

Based on this reasoning, the defect formation mechanism is as follows:

1. High strain rates occur at high rotation speeds, resulting in material toughness damage.
2. In the TCZ, the strain rate is the largest and the material toughness damage is more obvious.
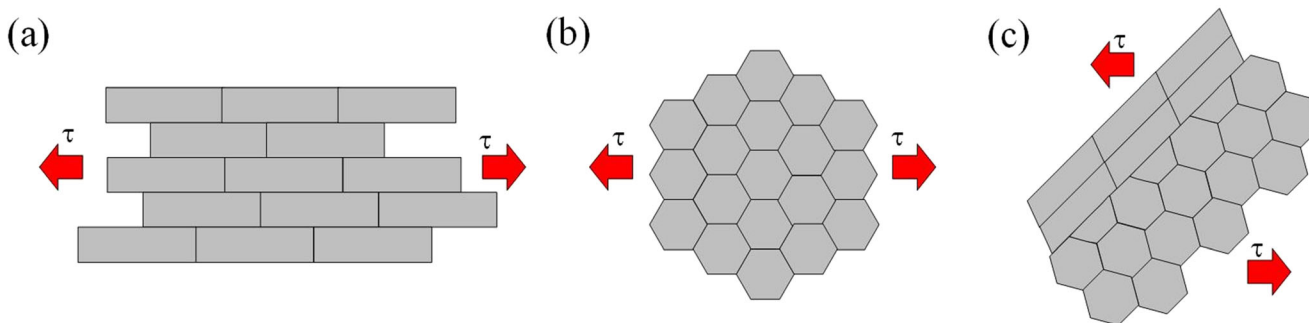
Fig. 11 Schematic diagram of the grain shear stress in the tensile test. **a** BM. **b** NZ. **c** TCZ

4.2 Fracture behaviour of crystals in different regions under tensile stress

Figure 11 shows a schematic diagram of the grain shear stress in the tensile test. Figure 11 a and b are associated with the grain orientation distribution of the fracture zone in BM and NZ. Figure 11 c shows a schematic diagram of the TCZ. When the grains in Fig. 11a are subjected to tensile stress, they slip along with the boundaries under the influence of arrangement behaviour (long-range order structure). The material undergoes plastic deformation, and the crystal lattice is distorted until cracking. The grains in Fig. 11b are sub-size equiaxed crystal with large boundaries. The dislocations slip to the vicinity of the boundaries and accumulate due to tensile stress. This causes dislocation block. There is a large angular deviation between grain orientation and the tensile direction in Fig. 11c. Meanwhile, material damage is more serious under the influence of high strain rate. It is inclined to fracture under the tensile stress [28].

5 Conclusions

SSFSW was used to weld 2219-T6 aluminium alloy at different rotation speeds. According to the present investigation on the microstructures and mechanical properties of the joints, the main conclusions are as follows:

(1) 2219-T6 aluminium alloy SSFSW joints have the characteristics of a smoother surface, narrower HAZ and TMAZ, uniform microstructure and no material loss.

(2) The plastic flow and strain rate of the weld increase with increasing rotation speed; this results in different grain orientations at the interface between AS and NZ. The TCZ is formed at the interface. The TCZ has the maximum strain rate at the welded joints. The plastic damage in the TCZ is obvious. Secondary sub-size voids aggregated to form cracks at 2600 rpm.

(3) The tensile strength of the joints decreases with increasing rotation speeds. The maximum strength is 305 MPa, equivalent to 68.2% of that of in BM. Furthermore, the lowest hardness is in the HAZ, while the softened regions are wider with increasing rotation speeds.

References

1. Mishra RS, Ma ZY (2005) Friction stir welding and processing [J]. Mater Sci Eng R Rep 50(1-2):1–7
2. Thomas WM, Nicholas ED (1997) Friction stir welding for the transportation industries. Mater Des 18(4-6):269–273
3. Davies PS, Wynne BP, Rainforth WM (2011) Development of microstructure and crystallographic texture during stationary shoulder friction stir welding of Ti-6Al-4V[J]. Metall Mater Trans A 42(8):2278–2289
4. Maltin CA, Nolton LJ, Scott JL (2014) The potential adaptation of stationary shoulder friction stir welding technology to steel. Mater Des 64:614–624
5. Ji S, Meng X, Ma L (2015) Vertical compensation friction stir welding assisted by external stationary shoulder [J]. Mater Des 68:72–79
6. Cho JH, Kim WJ, Lee CG (2014) Texture and microstructure evolution and mechanical properties during friction stir welding of extruded aluminum billets. Mater Sci Eng A 597(597):314–323
7. Sun T, Roy MJ, Strong D (2017) Comparison of residual stress distributions in conventional and stationary shoulder high-strength aluminum alloy friction stir welds [J]. J Mater Process Technol 242:92–100
8. Martin J P (2013) Stationary shoulder friction stir welding/ Proceedings of the 1st International Joint Symposium on Joining and Welding. Woodhead Publishing, pp 477–482
9. Wu H, Chen YC, Strong D (2015) Stationary shoulder FSW for joining high strength aluminum alloys. J Mater Process Technol 221:187–196
10. Sun T, Tremsin AS, Roy MJ (2018) Investigation of residual stress distribution and texture evolution in AA7050 stationary shoulder friction stir welded joints. Mater Sci Eng A 12:531–538
11. Li JQ, Liu HJ (2013) Effects of tool rotation speed on microstructures and mechanical properties of AA2219-T6 welded by the external non-rotational shoulder assisted friction stir welding. Mater Des 43:299–306
12. Li D, Yang X, Cui L (2014) Effect of welding parameters on microstructure and mechanical properties of AA6061-T6 butt welded joints by stationary shoulder friction stir welding. Mater Des 64:251–260
13. Hosain MM (2004) Development of high speed friction stir welding machine. Wichita State University
14. McNelley TR, Swaminathan S, Su JQ (2008) Recrystallization mechanisms during friction stir welding/processing of aluminum alloys. Scr Mater 58(5):349–354,064
15. Li B, Shen Y, Hu W (2011) The study on defects in aluminum 2219-T6 thick butt friction stir welds with the application of multiple non-destructive testing methods. Mater Des 32(4):2073–2084
16. Hu Y, Liu H, Fujii H (2019) Improving the mechanical properties of 2219-T6 aluminum alloy joints by ultrasonic vibrations during friction stir welding. J Mater Process Technol
17. Hu Y, Liu H, Li S (2018) Improving mechanical properties of a joint through tilt probe penetrating friction stir welding. Mater Sci Eng A 731:107–118
18. Gazder AA, Dalla Torre F, Gu CF (2006) Microstructure and texture evolution of bcc and FCC metals subjected to equal channel angular extrusion. Mater Sci Eng A415(1-2):126–139
19. Cao GKS (2005) Friction stir welding of 2219 aluminum: behavior of θ (Al2Cu) particles. Weld J 84(1):S1
20. Frigaard Ø, Grong Ø, Midling OT (2001) A process model for friction stir welding of age hardening aluminum alloys [J]. Metall Mater Trans A 32(5):1189–1200
21. Nielsen KL, Pardoen T, Tvergaard V (2010) Modelling of plastic flow localisation and damage development in friction stir welded

6005A aluminum alloy using physics based strain hardening law. Int J Solids Struct 47(18-19):2359–2370

22. Li D, Yang X, Cui L (2015) Investigation of stationary shoulder friction stir welding of aluminum alloy 7075-T651. J Mater Process Technol 222:391–398

23. Balmforth NJ, Frigaard IA, Ovarlez G (2014) Yielding to stress: recent developments in viscoplastic fluid mechanics. Annu Rev Fluid Mech 46:121–146

24. Goods SH, Brown LM (1979) Overview no. 1: the nucleation of cavities by plastic deformation. Acta Metall 27(1):1–15

25. Argon AS, Im J, Safoglu R (1975) Cavity formation from inclusions in ductile fracture. Metall Trans A 6(4):825

26. Song M, Kovacevic R (2003) Thermal modeling of friction stir welding in a moving coordinate system and its validation. Int J Mach Tools Manuf 43(6):605–615

27. Liu XC, Sun YF, Nagira T (2019) Strain rate dependent micro-texture evolution in friction stir welding of copper. Materialia 100302

28. Nielsen K L, Pardoen T, Tvergaard V (2010) Modelling of plastic flow localisation and damage development in friction stir welded 6005A aluminum alloy using physics based strain hardening law